



HAL
open science

Characteristics of the fluid–structure interaction within Darrieus water turbines with highly flexible blades

Stefan Hoerner, Shokoofeh Abbaszadeh, Thierry Maître, Olivier Cleynen,
Dominique Thévenin

► To cite this version:

Stefan Hoerner, Shokoofeh Abbaszadeh, Thierry Maître, Olivier Cleynen, Dominique Thévenin. Characteristics of the fluid–structure interaction within Darrieus water turbines with highly flexible blades. *Journal of Fluids and Structures*, 2019, 88, pp.13-30. 10.1016/j.jfluidstructs.2019.04.011 . hal-02126765

HAL Id: hal-02126765

<https://hal.science/hal-02126765>

Submitted on 12 Dec 2019

HAL is a multi-disciplinary open access archive for the deposit and dissemination of scientific research documents, whether they are published or not. The documents may come from teaching and research institutions in France or abroad, or from public or private research centers.

L'archive ouverte pluridisciplinaire **HAL**, est destinée au dépôt et à la diffusion de documents scientifiques de niveau recherche, publiés ou non, émanant des établissements d'enseignement et de recherche français ou étrangers, des laboratoires publics ou privés.

Characteristics of the Fluid-Structure Interaction within Darrieus Water Turbines with Highly Flexible Blades

Stefan Hoerner^{1 2}, Shokoofeh Abbaszadeh³, Thierry Maître², Olivier Cleynen¹, Dominique Thévenin¹

Accepted version of the article, published in the *Journal of Fluids and Structures* Volume 88, July 2019, Pages 13-30, doi: 10.1016/j.jfluidstructs.2019.04.011

Vertical-axis water turbines (VAWT), the target of the present study, provide a higher area-based power density when used in arrays, and are a promising alternative to horizontal-axis hydro-kinetic turbines (HAWT). Nevertheless, they operate under highly dynamic conditions near or even beyond dynamic stall at their best-efficiency-point. The abrupt loss of lift and strong increase of drag associated with hydrofoil stall can produce cyclic loads and possible damage of turbomachines due to material fatigue.

The effect of flexible structures in a highly dynamic flow regime including separation and stall is here studied systematically in an experimental setup which permits observations of all regimes ranging from quasi-static state up to the occurrence of deep dynamic stall and beyond. The process is studied using a surrogate model consisting of an oscillating NACA0018 hydrofoil in a closed water channel, following a motion law comparable to the real angle of incidence of a Darrieus turbine blade along its rotation. The investigated parameters are the oscillation frequency and tip speed ratio, for one rigid as well as for three flexible hydrofoils of different stiffnesses. The coupling process is therefore investigated for multiple machine designs and working points. Lift and drag measurements have been carried out in a systematic manner.

Results show that at tip speed ratios for which highly dynamic flow regimes occur, flexible blades provide not only higher thrust, but also reduced normal forces and reduced peak-to-peak cyclic normal force variations. This reduction of stress loads would translate into significantly increased turbine lifetime. This supports the need for further investigations in order to identify optimal blade flexibility and check further turbine designs.

¹Chair of Fluid Dynamics and Technical Flows, Institute of Fluid Dynamics and Thermodynamics, Otto von Guericke University Magdeburg, Universitätsplatz 2, D-39106 Magdeburg, Germany

²University Grenoble Alpes, CNRS, Grenoble INP*, LEGI, F-38000 Grenoble, France, *Institute of Engineering Univ. Grenoble Alpes

³Chair of Electric Drive Systems, Institute of Electric Power Systems, Faculty of Electrical Engineering and Information Technology, Otto von Guericke University Magdeburg, Universitätsplatz 2, D-39106 Magdeburg, Germany

Corresponding author: Stefan Hoerner, hoerner@ovgu.de

Nomenclature

\hat{c}_N	mean amplitude of the normal-force coefficient [-]	n	number [-]
α	angle of incidence [rad]	b	width of the foil [m]
α_{\max}	maximum angle of incidence [rad]	C	profile chord length [m]
α_{stall}	angle of incidence with onset of stall [rad]	\underline{F}_{xyz}	forces in xyz dimensions [N]
$\dot{\alpha}$	angular velocity of the pitching foil $\frac{d\alpha}{dt}$ [rad/s]	\underline{T}_{xyz}	torque in xyz dimensions [N m]
η	thrust-to-normal force ratio [-]	N	number of cycles before material failure [-]
λ	tip speed ratio, $\lambda = \frac{\omega_D R}{v_\infty}$ [-]	$\underline{R}_Z(\alpha)$	transformation matrix
ρ	density [kg/m ³]	Re	Reynolds number [-]
σ	solidity $\sigma = \frac{n \cdot C}{R}$ [-]	R	turbine radius [m]
θ	azimuth angle [rad]	S	stress [MPa]
$\underline{\omega}_D$	angular velocity of the turbine [rad/s]	s	profile planar area [m ²]
v_∞	free stream velocity [m/s]	T	normalized oscillation period [-]
\underline{w}	relative velocity [m/s]	t	thickness of the carbon blade [m]
c_D	drag force coefficient [-]	BEP	Best efficiency point
c_L	lift force coefficient [-]	DES	Detached Eddy Simulations
c_N	normal force coefficient [-]	FSI	Fluid-Structure Interaction
c_P	power coefficient [-]	HAWT	Horizontal Axis Water Turbine
c_T	thrust (tangential force) coefficient [-]	LES	Large Eddy Simulations
f_D	turbine rotor frequency [Hz]	PIV	Particle Image Velocimetry
f_o	oscillation frequency [Hz]	RANS	Reynolds-Averaged Navier-Stokes
k	reduced frequency [-]	RMS	Root mean square
k_D	reduced frequency of the turbine [-]	VAWT	Vertical Axis Water Turbine
k_o	reduced frequency of the oscillation [-]		
v_{ch}	channel inlet velocity [m/s]		
I	second moment of inertia [m ⁴]		

1 Introduction

Climate change and the greedy devour of our limited fossil resources since the beginning of the industrialization force us to change our global strategies of energy exploitation, heading towards renewable sources with sustainable technologies. Hydropower currently constitutes the largest share of renewable energies. Nevertheless, large dam systems, which provide high hydraulic head to improve the power density of hydropower systems, have a huge social and ecological impact, as reported very clearly by Rosenberg et al. [35], even if it is difficult to estimate the full range of this impact due to their complex far-reaching character [38]. In fact, even small-scale facilities obstruct fish migration. This issue is of recent research interest, bringing the need for theoretical performance considerations [34, 6] as well as assessment of fish passability [2, 3, 30].

Hydrokinetic turbines directly convert the kinetic energy of the flow and allow for a move away from dams and towards operation in very low-head flow conditions. However, the available energy for a free-stream installation is far lower as there is no potential energy which can be converted. Still, vertical-axis water turbines (VAWT), installed in marine currents and rivers could contribute to sustainable and environmentally -friendly hydropower exploitation. The most important advantage of VAWT is their area-based power density when used in farm configurations, which is reported to be significantly higher than for HAWT [41, 7, 4]. In sites with continuous flow directions, like rivers, a significant improvement of the rotor-based power coefficient can be achieved by collector constructions, as reported by Hashem and Mohamed for wind turbines [19]. The structure of a VAWT is quite simple, without need for guiding vanes or housing, but the flow conditions in the turbine are very complex: the blade angle of incidence α and relative speed \underline{w} , resulting from the velocity trian-

gle of free-stream velocity v_∞ and the tangential velocity of the blade ωR , vary constantly (fig. 1). Furthermore, VAWT blades operate under dynamic conditions including at least the onset of, or even deep dynamic stall. This is due to the high density of water, which requires a rotor with higher solidity σ compared to wind turbines. The consequences are smaller tip speed ratios λ and accordingly higher variations of the angle of incidence α in the best-efficiency point (BEP). For example, the turbine of the LEGI laboratory in Grenoble operates at $\sigma = 1.1$ and $\lambda_{\text{opt}} = 2$ [26]; the turbine studied by Zeiner-Gundersen with $\sigma = 0.9$ and $\lambda_{\text{opt}} = 2.2$ [42]. Those design points result in cyclic structural loads with small pulsing contributions to the thrust and multiple load peaks per turn. This is a general drawback of vertical-axis turbines and is known to cause damage due to material fatigue or defects on the main bearings [11, 31]. Only the sinusoidal component of the lift generates thrust (tangential force, see fig. 1). The cosine component is an order of magnitude higher and has to be compensated by the structure (normal force). The thrust-to-normal force ratio $\eta = c_T/c_{N_{\text{max}}}$, similar to the lift-to-drag ratio in aerodynamics, is a measure of the quality of the configuration, with higher values being desirable. Extreme working conditions, such as low tip-speed ratios, tend to lower η .

Increasing the value of η requires control of the occurrence of flow separation, which is related to phenomena such as vibrations and flutter caused by the negative damping in light stall, or the abrupt loss of lift and increase of drag in deep dynamic stall. Dynamic stall was extensively investigated in the field of helicopter aerodynamics during the 1970s and 1980s by McCroskey [27, 28]. This work was adapted to VAWT – which work under comparable conditions, as their angle of incidence α varies periodically with respect to azimuth angle θ – by Laneville and Vittecoq [21], who experimentally investigated the forces on a VAWT operating under dynamic stall conditions.

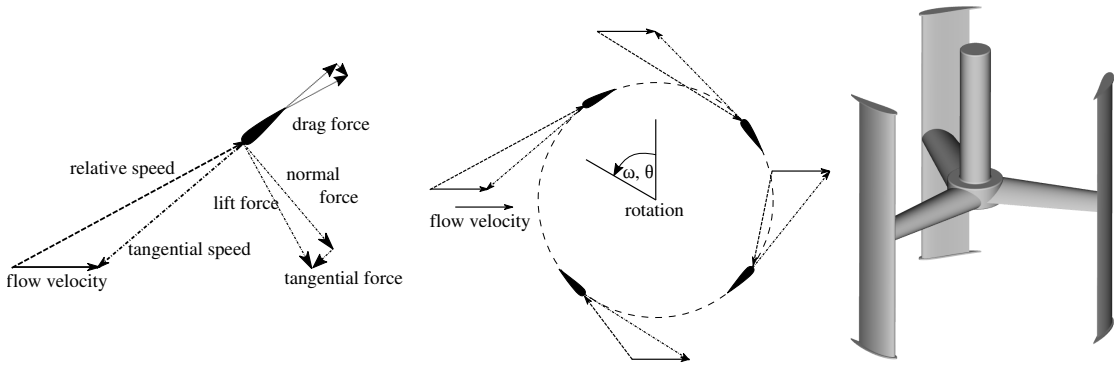


Figure 1: Left and middle: velocity triangles and hydraulic forces on a VAWT at $\lambda \approx 2.2$ for four azimuth angles: the angle of incidence varies with azimuth angle θ and tip-speed ratio. Only the tangential part (sinusoidal share) of the lift force generates thrust. Most of the hydrodynamic forces result in structural loads. Drag forces were scaled up for better readability. Right: CAD model of a three-bladed H-Darrieus turbine rotor.

Other experimental studies of the complex flow conditions in VAWT use Particle Image Velocimetry (PIV) to visualize the flow field [16]. Ferreira et al. [14] studied a one-bladed turbine at $Re \approx 100\,000$ with λ ranging from 2 to 4. In turn, Gorle et al. [18] studied a four-bladed turbine in a towing tank in comparable conditions. Gorle showed that for a very common tip speed ratio of 2, the flow remained attached for an azimuth angle θ of 50° to 100° , while dynamic stall occurred from 120° to 220° . The flow progressively reattached from 240° onwards, and a second vortex appeared between 0 and 40° (refer to fig. 1 for angles). Consequently, the flow was attached only 14% of the time in these operating conditions.

One approach to control the forces variation and raise the efficiency is to use an active or passive pitch mechanism for the blades, in order to adapt α along the azimuth angle θ . Active techniques may also improve self-starting capabilities. A detailed overview of the state-of-technology and its opportunities is given in Pawsey [33]. More recent studies mainly focused on decentralized actuator-based pitch [22, 43, 44] and optimizing the pitch trajectory [37].

The drawback of this approach is the mechanical or mechatronical complexity of the required system, which may need high maintenance efforts and is prone to failure.

Another approach to raise the single turbine efficiency is to optimize the blade shape. Recent studies show a possible improvement of more than 20% which can be obtained compared to a commonly-used symmetrical NACA profile by the use of computational fluid dynamics coupled with an optimizer using genetic algorithms [36, 10].

A third approach is to use an intelligent design featuring structural flexibility. It is known from bionic studies that whales raise the efficiency of their fins through flexibility [15]. Adjusted flexible structures can adapt to the flow by deformation. Flexible compound structures can naturally reproduce this effect by adapted stiffness which can be set by design. This was demonstrated experimentally and numerically by McPhee and Beyene, first for horizontal-axis wind turbines [24], later also for vertical-axis wind turbines through numerical analysis, with promising results [25].

VAWT is a challenging task for numerical simulations. Reynolds-Averaged Navier-

Stokes (RANS) simulations with fully-modeled turbulence and wall functions for the boundary layer can provide quite accurate power predictions in the turbine best-point [26] and show good accordance for the forces integrated over the whole blade [12], but have strong dependency of the chosen turbulence model and grid refinement [8] while the shear stress transport $k-\omega$ model is considered to be most suitable for VAWT [17]. They may fail at low λ when deep dynamic stall is the governing flow regime. They are also known to badly reproduce key aspects of the flow field, in particular boundary layer separation [12, 9, 8]. Separation is often overestimated and the point of occurrence shifted in time (and so in θ). RANS-based, two-way strongly-coupled simulations of the fluid-structure interaction (FSI) on highly deformable VAWT structures might capture these high dynamic flow conditions. However, they may not always provide very reliable results, since the position of the separation point and the load (pressure) distribution on the blade both strongly influence the behavior of such flexible structures. Three-dimensional Large-Eddy Simulations (LES) or Detached-Eddy Simulations (DES) appear to be significantly more accurate, but remain computationally extremely challenging [13, 32]. Such simulations are almost impossible on current supercomputers when two-way FSI is involved and the algorithm enters, for each time step, an internal loop for structure deformation versus flow pressure distribution [39]. Another issue is the mesh deformation, which can be challenging at the fine mesh resolutions required for LES.

This explains the necessity of further experimental investigations, as an essential source of information. Zeiner-Gundersen presented an experimental study with deformable blades on a 5-bladed low- λ VAWT with promising results [42]. The flexibility improved self-starting capabilities, raised the efficiency, and shifted the BEP to lower values of λ . One last advantage is the in-

crease in fish-friendliness of the device associated with lower rotational speeds [30].

The objective of the present study is to experimentally investigate the two central questions: Can flexible structures 1) lower the cyclic structural load, and 2) perhaps even improve the efficiency of vertical-axis water turbines?

2 Modeling

In order to simplify the experimental setup for the study, the VAWT is replaced by a surrogate model, which allows to precisely study the influence of structure flexibility concerning the occurrence of dynamic stall. This is the dominant issue for working points at low λ , which are particularly interesting for VAWT with low ecological impact. All secondary effects like tip and strut effects or blade-blade interaction, which become important at higher λ [8], are neglected.

The two targets of the study –lifetime and efficiency– are quantified using the maximum normal force (non-dimensionalized as the average amplitude of normal coefficient \hat{c}_N), the thrust efficiency η , and the tangential force (non-dimensionalized as the thrust coefficient c_T).

The amplitudes of the cyclic loads (normal force) are a crucial factor for the turbine lifetime. High-cycle fatigue analysis based on $S - N$ diagrams relates the number of cycles before fatigue failure N to magnitude S of the stress peaks. In such an analysis, it is known that N increases exponentially when S is lowered [5]. The amplitude of the normal coefficient (\hat{c}_N) (see eq. 9) can be seen as an equivalent, as S is proportional to it.

The tangential force delivers the turbine torque and serves to compare the benefit of different levels of flexibility for a given turbine design and operating point (eq. 7). The thrust-to-normal force ratio η is a benefit-to-cost ratio in this study.

For the surrogate model, a single-bladed VAWT is considered as an oscillating hydrofoil (fig. 2). This concept was used al-

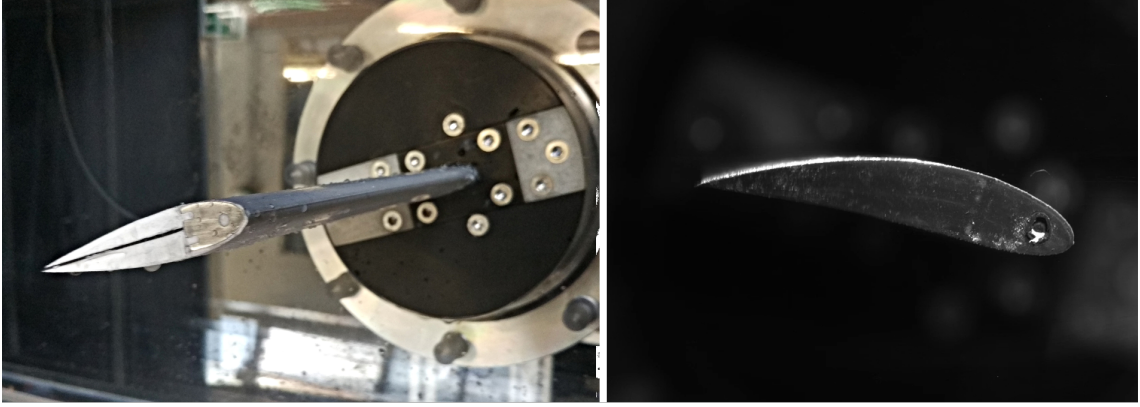


Figure 2: Left: The compound hydrofoil consists of a leading edge milled from aluminum, a skeleton of carbon and a body of silicone. The rigidity of the foil is adjustable through the thickness of the carbon core. It is mounted on a six-axes load cell via an aluminum base plate. Right: The most flexible design (carbon blade thickness 0.3 mm) performs large deformations during one period. The picture shows the deflection for the $\lambda=3$ case at $\alpha = 20^\circ$

ready in other studies such as that of Ly et al. [23]. As a consequence of this approach, some characteristics of real VAWT are not taken into account. Strut and tip losses, as well as blade-blade interaction, are not present. The model does not reproduce the upstream-downstream and blade-wake interactions. Therefore, values for thrust are expected to be raised artificially, especially in the downstream part of the path. Further quantitative studies will have to take those complex flow characteristics into account.

Also, in the present case, the flow velocity w , which is alternating in real turbines, must be kept constant in the closed-loop water channel used for this study. This will result in a constant Reynolds number. However, McCroskey showed that the influence of Re is small for a fully turbulent flow. This was also true for the normal force and the vortex shedding [29].

A dominant factor to determine the flow conditions on the blade is the tip speed ratio λ . It is defined as the ratio of blade tangential speed $\omega_D R$ to free-stream speed v_∞ :

$$\lambda = \frac{\omega_D R}{v_\infty} \quad (1)$$

Eqs.2-4 below describe the motion and the flow for such a blade. Using λ and the rotor's azimuth angle θ , the angle of incidence α follows a trajectory for the non-sinusoidal oscillation of a blade (fig. 3) that is given by:

$$\alpha = \arctan \left(\frac{\sin \theta}{\lambda + \cos \theta} \right) \quad (2)$$

Then, as shown by Laneville et al. [21], the angular velocity $\dot{\alpha}$ of the pitch motion can be calculated with respect to the angular velocity of the turbine ω_D , λ and θ :

$$\dot{\alpha} = \frac{\omega_D (1 + \lambda \cdot \cos \theta)}{1 + 2\lambda \cdot \cos \theta + \lambda^2} \quad (3)$$

The alternating relative flow speed on the blade of a VAWT w is obtained with eq. (4) and depends on v_∞ , λ and θ :

$$w = v_\infty \sqrt{1 + 2\lambda \cos \theta + \lambda^2} \quad (4)$$

In order to transfer this approach into an oscillating airfoil experiment in a closed water tunnel, the inlet speed becomes the relative flow speed and is set constant. Therefore, the root mean square (RMS) of the

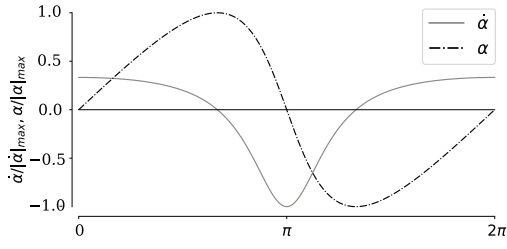


Figure 3: Normalized angle of incidence α and pitch speed $\dot{\alpha}$ for $\lambda=2$. The non-harmonic trajectory leads to a maximum absolute pitch speed in the descending branch. This has to be considered in the definition of k_D and k_o .

relative flow speed along one turn of the rotor is set as v_{ch} for the channel in the experiment. It corresponds to the average inlet speed and is given by volume flow rate divided by the channel cross-section. The thrust coefficient c_T , the normal force coefficient c_N (and its amplitude \hat{c}_N) can be calculated from c_L and c_D (fig. 4):

$$c_D = \frac{F_D}{0.5 \cdot \rho \cdot s \cdot v_{ch}^2} \quad (5)$$

$$c_L = \frac{F_L}{0.5 \cdot \rho \cdot s \cdot v_{ch}^2} \quad (6)$$

$$c_T = c_L \cdot \sin \alpha - c_D \cdot \cos \alpha \quad (7)$$

$$c_N = c_L \cdot \cos \alpha + c_D \cdot \sin \alpha \quad (8)$$

$$\hat{c}_N = \frac{c_{N_{max}} - c_{N_{min}}}{2} \quad (9)$$

Those coefficients will allow to compare the experimental results of the flexible hydrofoils with those of the rigid foil reference (see section 3).

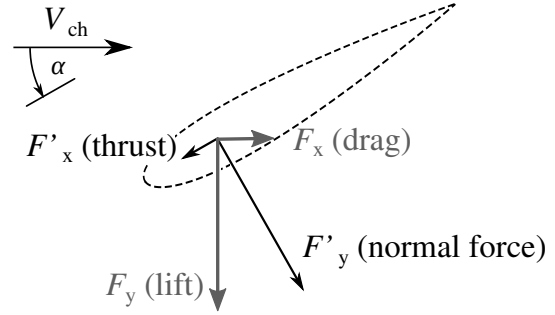


Figure 4: Reference frame of the measurement with qualitative forces and coefficients. Thrust and normal loads are the sinusoidal and cosine shares of lift and drag. v_{ch} becomes equivalent to the relative velocity w . The measured forces and moments F'_{xyz} , M'_{xyz} from the rotating sensor get transformed to the channel coordinate system and become F_{xyz} and M_{xyz} (see sec.3)

The flow regime on the blades depends strongly on λ and on the solidity σ of the turbine. The definition of σ is not uniform in literature; it is often based on the diameter, but sometimes on the radius. In line with former studies at the LEGI laboratories, a convention conformal to [26] is used: the solidity is then defined as the ratio of the plan view area of the blades to half of the turbine's cross-section area:

$$\sigma = \frac{n \cdot C}{R} \quad (10)$$

These two parameters can be combined into a non-dimensional number, the reduced frequency k_D , which determines the stall behavior of the flow in a VAWT. It relates the ratio of the time scale of the vortex convection over a profile to the time scale of the profile motion. Starting with k , from helicopter aerodynamics [27] (eq.(11), left), then specifically for a blade in a rotating reference frame [21] (eq.(11), right), the reduced frequency k_D for a VAWT is given by eq.(12) from Laneville and Vittecoq [21]. In

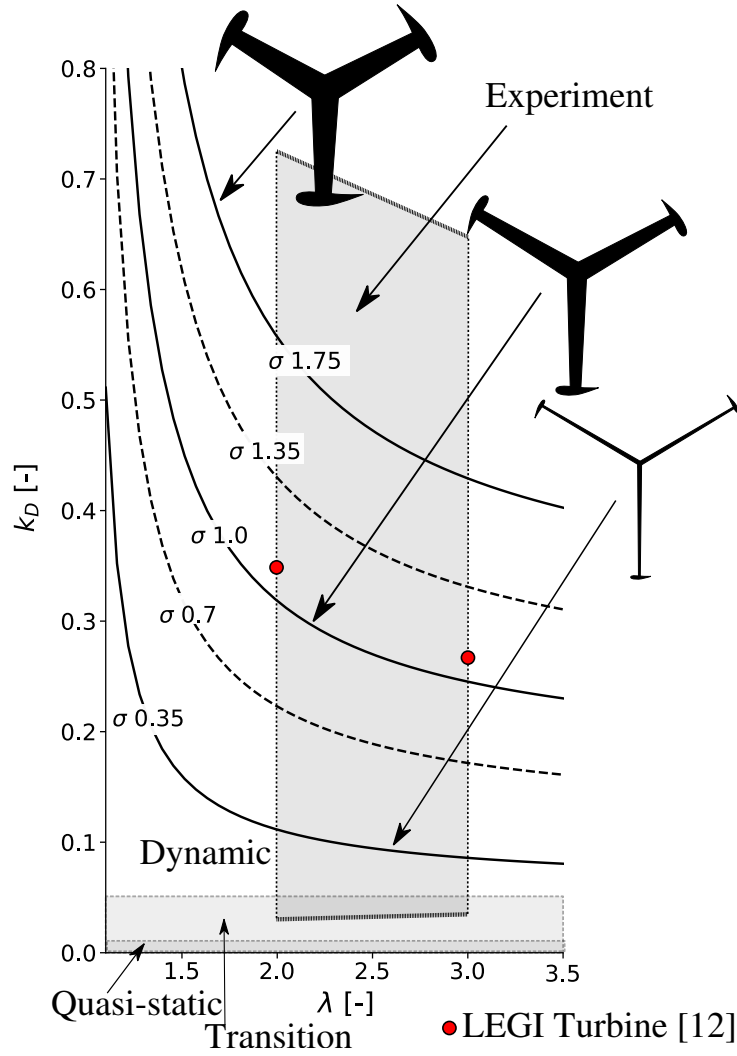


Figure 5: Influence of λ and k_D on turbine design, and region investigated in this study. Thin structures with high λ are characterized by low k_D , while massive structures with low λ lead to high k_D . The value of k_D diminishes with increasing λ as the maximum angle reduces; while k_D increases with raising solidity as the relation of the chord length C to the turbine radius R grows. For visualization purposes, solidity σ is calculated here for a three-bladed turbine, k_D and k_o include C/R (see eqs.(10)&(12)).

the case of a non-symmetric motion trajectory, $\dot{\alpha}$ is the absolute pitch speed. That is the reason for $\lambda - 1$ instead of $1 - \lambda$ in the denominator of eq. (12) which leads to positive k_D even if $\dot{\alpha}_{max}$ is in the descending pitch motion (fig. 3).

$$k = \frac{C \cdot \dot{\alpha}_{max}}{2v_{\infty} \cdot \alpha_{max}} = \frac{C \cdot \dot{\alpha}_{max}}{\omega_D \cdot 2R \cdot \alpha_{max}} \quad (11)$$

$$k_D = \frac{C}{2 \cdot R \cdot (\lambda - 1) \cdot \arctan \left[(\lambda^2 - 1)^{-\frac{1}{2}} \right]} \quad (12)$$

The rotor frequency is given by the angular velocity ω_D (eq.(13 left)). Considering now the case of an oscillating profile in a tunnel, the average oscillation frequency f_o can be calculated from the oscillation period T_{osc} (eq.(13 right)) which connects the turbine rotation to the profile oscillation:

$$f_D = \omega_D/2\pi = f_o = \frac{1}{T_{osc}} \quad (13)$$

However, the angular velocity $\dot{\alpha}$ of the profile is not constant. In this case f_o alone is not sufficient to characterize flow dynamics from the forced oscillation. Therefore, the reduced oscillation frequency k_o is more adequate. k_o is introduced inserting eq.(2) and eq.(3) into eq.(11)-right, which leads to eq.(14):

$$k_o = \frac{\pi \cdot f_o \cdot C}{v_{ch} \cdot (\lambda - 1) \cdot \arctan \left[(\lambda^2 - 1)^{-\frac{1}{2}} \right]} \quad (14)$$

This formulation of k_o accounts for the non-sinusoidal shape of the evolution of α with respect to time. The sawtooth-like curve depends on the value of λ (see eq.(2)) and has a very strong influence on the unsteady effects characterizing the flow.

In both equations 12 and 14, the case of $\lambda=1$ leads to a singularity with infinite k (fig. 5), as α jumps from 90° to -90° at $\theta = \pi$

(see eq.(2)):

McCroskey showed that the reduced frequency is a crucial parameter for the stall dynamics. A NACA0012 behaves at $k=0.004$ almost quasi-static, while the characteristics corresponds to dynamic stall at $k=0.06$ upwards [27]. These characteristics depend on the maximum angle, as well as the foil geometry. For the given experimental setup, the quasi-static characteristics were found for $k_o < 0.01$ and the fully dynamic state was reached for all sets at $k_o=0.06$.

The parameter k_D includes the ratio of chord length C to the turbine radius R and links it to the tip speed ratio λ . The latter defines the operating point of the turbine. The oscillation frequency f_o substitutes R in k_o . This allows to cover an entire field of turbine designs by the variation of only two parameters: 1) the reduced frequency k_o and 2) the tip speed ratio λ . Their influence is mapped in fig. 5. This feature will be used in the experiments to cover the range relevant for most common VAWT designs.

3 Experimental Setup

A set of NACA0018 hydrofoils is investigated in the study: three flexible variants are investigated, along with a fully-rigid milled aluminum foil for reference. The flexible foils consist of a milled aluminum leading edge, in which a carbon composite blade is inserted along the length of the foil (fig. 2). Three values for the blade thickness t are investigated: 0.3, 0.5 and 0.7 mm. The stiffness of the foil grows with t^3 , since the second moment of inertia I reads:

$$I = \frac{b \cdot t^3}{12} \quad (15)$$

The silicone embodiment has a Young's modulus 1.5×10^5 times smaller than that of the carbon composite, so its contribution to the overall stiffness is neglected. Structural effects like strain hardening of silicone

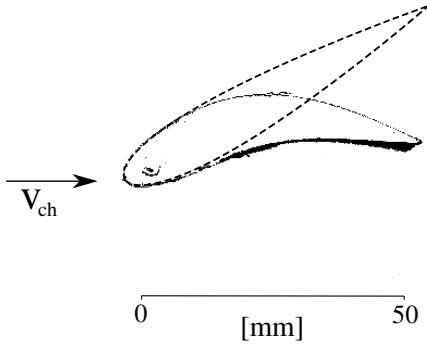


Figure 6: Experimentally-measured deflection of the flexible foil (for $t=0.3\text{mm}$) at $\lambda=2$ and angle of incidence $\alpha = 30^\circ$. The acquisition was made with a Phantom V2511 high-speed camera, colors were inverted, and the non-deformed shape for the same position was later added to the plot. The deformation changes the shape of the foil; in consequence it behaves like a high-cambered foil operating at lower angle of incidence.

polymers under cyclic loads with high frequency, as well as the influence of the blade natural frequency and damping, are the subject of ongoing investigations by the authors and are neglected in this first work.

Each foil is placed in a closed-loop water channel at LEGI Grenoble (fig. 2). A forced rotational oscillation is generated with a 5 kW servo drive system, following the trajectory defined by eq.(2). Hydrodynamic forces produce large deformations of magnitude 25 mm for a foil with 66 mm chord length (fig. 6). They are measured with a fully-submerged, six-axes load cell underneath a base plate on which the hydrofoil is mounted. The sensor rotates along with the foil leading edge. The pivot point is placed at quarter chord (fig. 7).

The rotated six-axes load-cell provides thrust and normal force. Then, a transformation matrix $\underline{R}_Z(\alpha)$ is applied to project the forces and the torque to the static (earth) reference frame and to obtain lift

and drag:

$$(\underline{F}, \underline{T})_{xyz} = \underline{R}_Z(\alpha) \times (\underline{F}', \underline{T}')_{xyz} \quad (16)$$

with

$$\underline{R}_Z(\alpha) = \begin{bmatrix} \cos \alpha & \sin \alpha & 0 \\ -\sin \alpha & \cos \alpha & 0 \\ 0 & 0 & 1 \end{bmatrix} \quad (17)$$

The experimental parameters for the setup were chosen in order to achieve results comparable with those from previous studies on a VAWT model at LEGI [26]. This VAWT model is subsequently called LEGI turbine:

Geometrical similarity:

The LEGI turbine is built with 4% cambered NACA4518 alike hydrofoils. These follow the flow curvature of the rotational motion of the turbine blades [1]. In the present experiment they are replaced by a symmetric NACA0018, since the flow in the channel has no rotational component.

Reduced frequency:

The range of tip speed ratio was set to $\lambda = [2, 3]$. This leads to angles of attack $\alpha_{\max} = [20^\circ, 30^\circ]$. The resulting reduced frequency for the LEGI turbine varies between $k_D = 0.26$ at $\lambda = 3$ and $k_D = 0.35$ for $\lambda = 2$ [26]. Due to sensor stiffness, the maximum frequency that could be achieved in the present study was $f_o = 6.45$ Hz. Higher frequencies would lead to sensor damage through resonance. This limited the maximum achievable range to $k_o = 0.71$ for $\lambda = 2$ and $k_o = 0.653$ for $\lambda = 3$ (see fig. 5).

Chord-based Reynolds number:

Re is a function of the azimuth angle θ for VAWT, the (fixed) experimental Reynolds number was chosen to correspond to the RMS(Re) along one revolution (Re=200 000). A flow speed of $v_{\text{ch}} =$

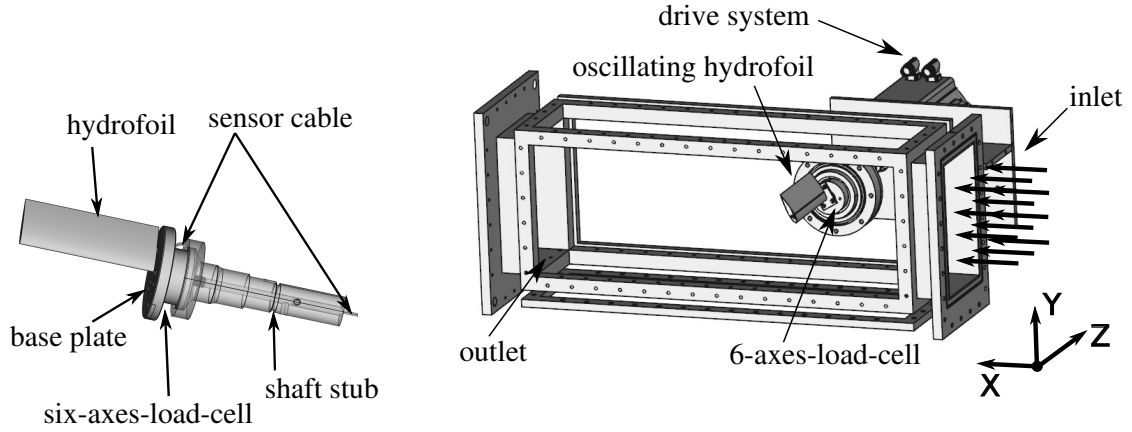


Figure 7: Experimental setup: Left: Detail of shaft, sensor and foil; right: test section at LEGI Grenoble with a streamwise length (X -axis) of 1000 mm, a spanwise width (Z -axis) of 175 mm and a height (Y -axis) of 280 mm. The closed water channel can run up to 600 l s^{-1} volume flow rate. The foil rotation center, at $1/4$ chord length, is placed 300 mm downstream of the inlet.

3.5 m s^{-1} in the water channel leads to a profile chord length $C = 0.066\text{ m}$. For the flexible foil ($t=3\text{ mm}$) case (inlet velocity was set 3.0 m s^{-1}) the variations remain below 1% of the average velocity and are considered negligible. v_{ch} is measured with the forces/moments for each data point at 1 kHz acquisition rate. k_o was calculated using the average value of v_{ch} for each period and then averaged.

Confinement:

The maximum blockage ratio can reach up to 12% (for the rigid foil, at a maximum angle $\alpha_{\text{max}} = 30^\circ$). This value exceeds 6%, which is considered a safe limit for a negligible influence [40]. However, confinement results in higher lift forces. On flexible foils, the deformation of the blade tends to decrease blockage for high angles of incidence (as can be seen in fig. 6).

Measurement equipment, filtering and uncertainty:

All experiments have been repeated twice in an independent manner, with no notice-

able differences. In consequence any remaining measurement errors are considered to be systematic.

The experiment is controlled with a purpose-built Python-based environment. To achieve accurate set point control, an Ethernet-based communication with the drive system was implemented using the Telnet protocol. The implemented algorithms allow to perform arbitrary periodical motion for a given trajectory.

A low-cost acquisition card (lab-jack T7 pro) collects and streams the data with 1 kHz sample rate at 16 bit accuracy for volume flow rate, temperature, three forces, three moments, position feedback and an external trigger signal.

The data is filtered with a hardware-based R/C filter with a 480 Hz low pass, to prevent aliasing and to eliminate noise from the power inverter. No further filtering or signal software-based postprocessing was necessary.

The set point precision of the drive system is given with 0.058° (by 0.0439° resolver resolution, as the zero angle was set with 0.014° accuracy 0.25 mm m^{-1} with a water level).

Standard weights were used to determine the static accuracy of the load-cell-based force measurement system. The maximum error was found to be less than 0.009% to full scale (800 N) and from 0.05% to 4.8% relative error when calibrating with loads from 2 kg to 0.1 kg mass load. In consequence the static load uncertainty is considered negligible for a single-axis load in the range of the experiment with $-200 \text{ N} < F_y < 200 \text{ N}$ and $0 \text{ N} < F_x < 100 \text{ N}$.

However, significant crosstalk is specified by the manufacturer: from 0.3% of full scale 800 N (y to x and conversely) to 1.82% of 1600 N (for z to x). Also, the dynamic characteristics of the sensor (0.26% hysteresis on full scale of 800 N for x and y) raise the uncertainty. In summary, the signal for the dynamic drag measurements without profile stall has to be taken in the range of the uncertainty.

In a second step, the static lift and drag coefficients for the system were captured with and without water; the results of the difference between them—the hydrodynamic forces—for the rigid hydrofoil were compared to computed results produced with the JavaFoil utility [20]; the results are displayed in fig. 8. Measurements and calculations are consistent below the static stall angle. However the slope of the experimental lift curve is less steep and the drag curve is shifted to lower magnitudes. The differences remain $<1\%$ of the sensor full scale and the effect on the drag can be explained by the sensor crosstalk.

Since JavaFoil is not able to predict accurate results in the stall region, no lift and drag coefficients were computed there.

Table 1 will give an overview of the experimental parameter:

4 Results

The experiment begins with a quasi-static/transitional low-frequency case of $f_o = 0.22 \text{ Hz}$. The frequency is then raised in seven steps up to 5.71 Hz for $\lambda=2$. For $\lambda=3$, eight steps were performed up to a fre-

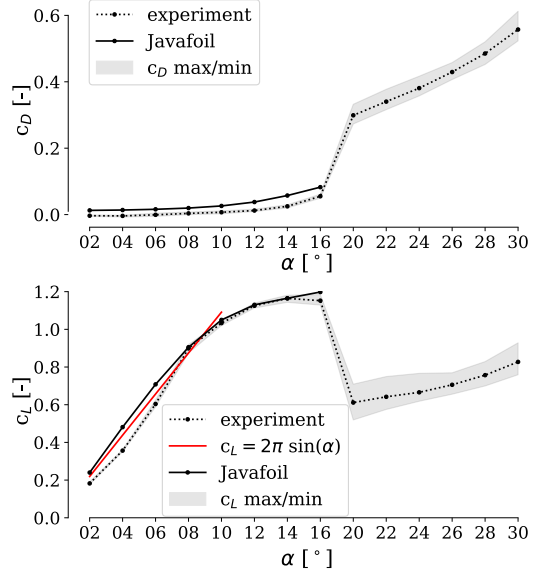


Figure 8: Comparison of the experimental measured drag (top) and lift (bottom) coefficients with calculated values. The grey fields are the min/max variations from mean value. The results show satisfactory agreement with Javafoil and with the theoretical slope ($c_L = 2\pi \sin(\alpha)$) below the static stall angle of $\approx 15^\circ$.

Table 1: Parameters of the experiment

	Symbol	unit	value
Tip-speed ratio	λ	–	[2.0, 3.0]
Composite plate thickness	t	m	[0.3, 0.5, 0.7]
reduced frequencies ($\lambda=2$)	k_o	–	[0.03, 0.06, 0.16, 0.28, 0.33, 0.46, 0.71]
reduced frequencies ($\lambda=3$)	k_o	–	[0.03, 0.07, 0.13, 0.24, 0.34, 0.49, 0.62, 0.65]

quency of 6.45 Hz. In both cases, an upper limit was set on f_o in order to prevent resonance damage on the load cell. The oscillation was performed over 10 s for each step. Figures 9-10 display the lift and drag coefficients over one normalized oscillation period T for $\lambda=2$, and figs.13-15 display those same values for $\lambda=3$. The upper plot (lift coefficients over one period) also includes the trajectory of the angle of incidence, which is plotted unitless ($[\circ/10^\circ]$) to fit with the lift coefficients. The plot maps the mean values for all normalized periods within the measurement time of 10 s, with the first and last periods excluded. Only a selection of the investigated frequencies is shown, including minimum, intermediary and maximum values for k_o . Variations of the inlet velocity v_{ch} lead to differences in k_o for constant f_o . This means that k_o is the mean frequency for each frequency step.

4.1 Results for $\lambda = 2$

4.1.1 Transitional state at $k_o = 0.026$ (fig. 9 (left)):

Rigid hydrofoil: From starting point $\theta = 0$ the lift increases with the angle of incidence until the static stall angle of $\alpha=15^\circ$ ($c_L=1.4$). The lift remains constant until it suddenly decreases to $c_L=0.8$ at $\alpha=19^\circ$ after a short peak to $c_L=1.7$. It then remains almost constant with further losses after α_{max} is reached; a small positive peak is visible when the flow reattaches at $\alpha=7.5^\circ$. At the zero-crossing (when the profile becomes horizontal), c_L is zero. The drag coefficient c_D is very low for $\alpha < \alpha_{stall}$ and remains in the range of the measurement uncertainty. When the stall point is reached, c_D displays

a large peak and then remains at a high value, increasing until α_{max} is reached. The drag then steeply decreases until the flow reattaches: There again c_D becomes lower than the measurement uncertainty.

Flexible hydrofoils: The flexible foils provide a smoother trend than the rigid foil. None of the three foils feature a pointed peak, on either the lift or the drag curves. Apart from the area close to the stall point, all flexible foils display values of c_L similar in magnitude to those of the rigid foil, while their values for c_D are significantly reduced in the stalled regime.

Similar trends are observed for both rigid and flexible foils in the second half of T . Compared to the first half of the motion, the magnitude of both $c_L =$ and c_D is increased, as is the stall angle. This is due to the different motion $\dot{\alpha}$ (quantified by eq. 3 and visible in fig. 3 and as the slope of the black curve in figs. 9-10).

4.1.2 Dynamic stall at $k_o = 0.277$ (fig. 9 (right)):

Rigid hydrofoil: With this increase in k_o , the stall angle is raised very significantly ($\alpha_{stall} = 27^\circ$, $c_{L,max} = 2.7$). Past this angle, the loss of lift is less pronounced than for lower k_o ; however, a hysteresis loop becomes visible and the flow does not seem to reattach before the shift in direction. At zero-crossing, c_L already takes the value -1.5. The point of no lift α_{zl} is reached at $\alpha_{zl}=12^\circ$ in the descending and $\alpha_{zl}=-10^\circ$ in the ascending motion. Thus, the lift trajectory is shifted leftwards with respect to α . In the meantime, the integral of the lift for one period increases.

The drag curve also changes significantly:

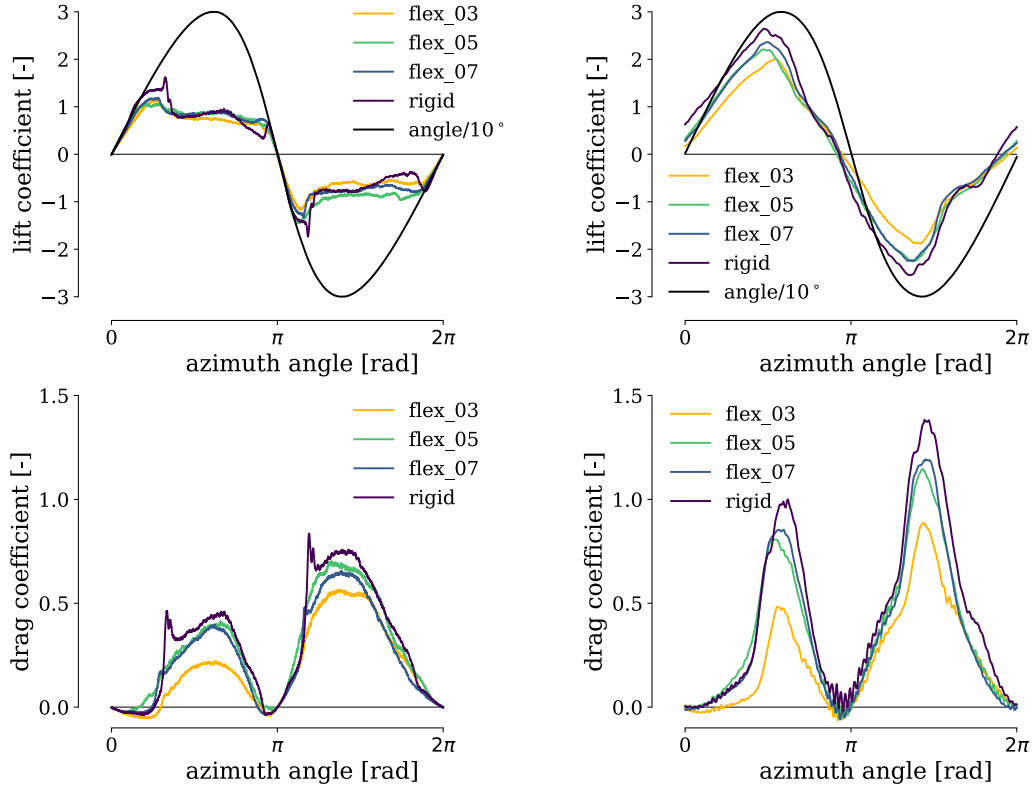


Figure 9: Results at $\lambda=2$ for four NACA0018 hydrofoils: one rigid and three flexible foils with different blade thicknesses: [0.3, 0.5, 0.7] mm. The black sinusoidal curve in the upper plots displays the angle of attack α [$^{\circ}/10^{\circ}$], with $\alpha_{\max}=30^{\circ}$. Left: Transitional state at $k_o=0.026$; Right: Full dynamic state with deep dynamic stall at $k_o=0.277$;

the characteristic spike with onset of stall disappears, while the two maxima are increased and display a slender shape. The hysteresis concerning lift does not appear for drag. The drag coefficient peaks at 1.0 in the descending branch (at $\alpha=27^{\circ}$) and at 1.5 in the ascending branch (at $\alpha=-28.5^{\circ}$).

Flexible hydrofoils: All flexible foils display less lift than the rigid foil. The integral of the lift over the trajectory is lower and it decreases together with the stiffness. The stall angle is increased, with the most flexible foil ($t=0.3$) achieving $c_{L_{\max}}=2$ at $\alpha_{\text{stall}}=29^{\circ}$.

The drag curves display similar behavior to those of the rigid foil. Nevertheless, the drag is everywhere lower, and the maxima are re-

duced by 25 to 50% compared to those of the rigid foil.

4.1.3 Dynamic stall at $k_o = 0.46$ (fig. 10 (left)):

For all foils, for both lift and drag, some weak oscillations begin to appear.

Rigid hydrofoil: As the reduced frequency is increased, the stall angle increases to reach $\alpha_{\text{stall}}=29^{\circ}$. However, the lift coefficient never exceeds $c_{L_{\max}}=2.7$. Peaks in the drag coefficients which were observed at lower frequencies diminish.

Flexible hydrofoils: All three foils follow the trend described above. The two most rigid foils ($t=0.5$ and 0.7 mm) have lift

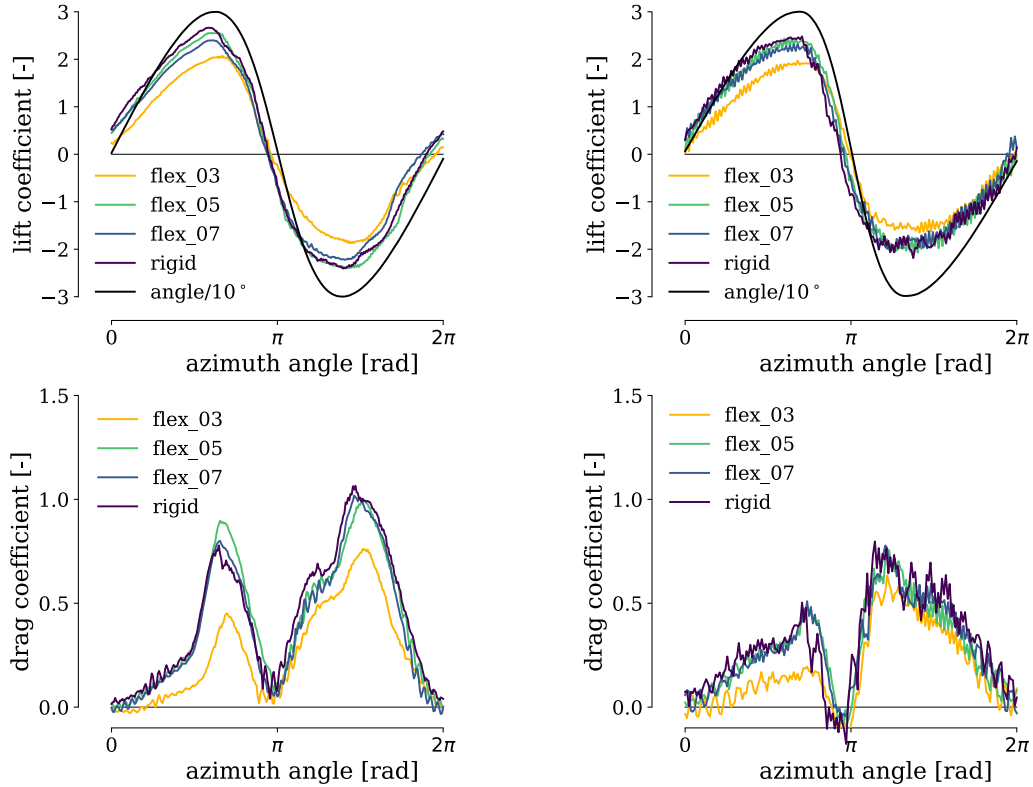


Figure 10: Results at $\lambda=2$ for four NACA0018 hydrofoils: one rigid and three flexible foils with different blade thicknesses: [0.3, 0.5, 0.7] mm. The black sinusoidal curve in the upper plots displays the angle of attack α [$^{\circ}/10^{\circ}$], with $\alpha_{\max}=30^{\circ}$. Left: Fully-dynamic state at $k_o=0.46$; Right: Fully-dynamic state at $k_o=0.71$.

and drag curves almost identical to those of the rigid foil. For the most flexible foil, maximum lift occurs past the maximum angle of attack, and the curve is close to zero at both zero-crossings, suggesting that hysteresis, one indicator for dynamic stall, vanishes with higher k_o .

4.1.4 Dynamic state at $k_o = 0.71$ (fig. 10 (right)):

Larger high-frequency oscillations are now observed for all curves and all foils. It is possible that the natural frequency of the multi-mass system containing the sensor, the base plate and the hydrofoil (fig. 7), is approached. A light dynamic stall with negative damping [28] may also play

a role. Those effects are under further investigation, requiring deeper knowledge of the structural properties and especially of the flow field.

Rigid hydrofoil: There are only light indications of stall, in the descending branch, with $c_{L_{\max}}=2.5$ at $\alpha_{\text{stall}}=30^{\circ}$. Compared to the previous (lower) frequency, the maximum drag is significantly reduced.

Flexible hydrofoils: As for the rigid foil, stall indicators become less dominant. The loss of lift and the overshoot of drag are shifted to higher azimuth angle, while the hysteresis loop becomes narrower.

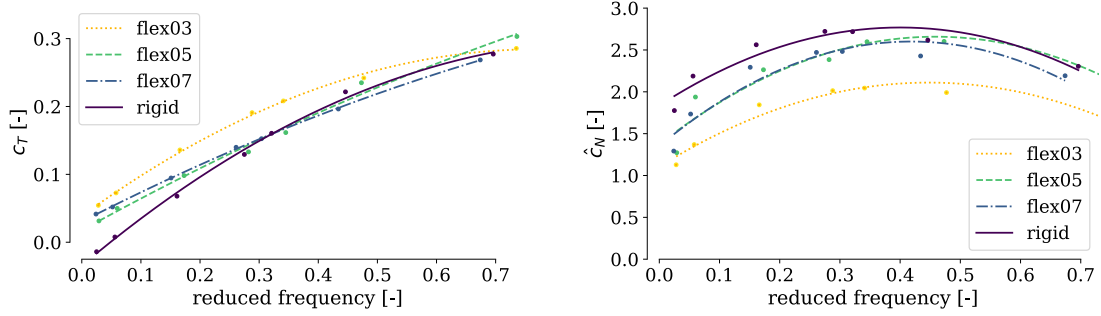


Figure 11: Left: Thrust coefficient c_T , a measure for the qualitative performance, as a function of reduced frequency. Right: Amplitude of the normal coefficient (\hat{c}_N), an indicator for the turbine lifetime, as a function of the reduced frequency k_o . Lower values are favorable, since lifetime rises exponentially with diminishing stress; A second-order polynomial curve fit of the data was added. These results correspond to $\lambda=2$ for four NACA0018 hydrofoils: one rigid and three flexible foils with different blade thicknesses: [0.3, 0.5, 0.7] mm.

4.1.5 Performance and lifetime improvements

The relationship between reduced frequency and thrust coefficient is shown in fig. 11(left). It displays the average thrust coefficient for one rotor revolution as a function of reduced frequency. It can be seen that the most flexible hydrofoil performs best, with significant improvement compared to the rigid reference especially in low- k_o region. The effect becomes less important with higher k_o . A maximum could not be obtained for these curves, maybe due to the experimental limitations on the oscillation frequency. The model allows to examine the effect of flexibility in specific design points, one for each k_o . The comparison between two k_o or design points is not possible in this model. In this case, the power output c_P would have to include the turbine radius (which grows with raising k_o as the chord length is constant) and further parameters like secondary effects as tip losses or blade-blade interaction, which is not possible with the current measurements. For $k_o=0.71$, the intermediate flexible foil ($t=0.5$ mm) overperforms the most flexible one ($t=0.3$ mm). This indicates that the optimal stiffness is

related to k_o , but demands further investigations. The LEGI turbine model with BEP at $\lambda=2$ has a $\sigma=1.1$ and so a value of $k_D=0.35$ [26]. At this operating point ($k_o=0.35$), the most flexible hydrofoil ($t=0.3$ mm) provides best performance with 20% improvement of thrust compared to the rigid reference.

The influence of foil stiffness on the turbine lifetime is displayed in fig. 11(right), which displays the mean amplitude of the normal force coefficient, \hat{c}_N (see eq. 9), as a function of the reduced frequency. The trend is parabolic for all foils. It becomes obvious from this figure that flexibility can contribute to lower structural loads compared to the rigid reference, decreasing the cyclic stress, which translates into exponential increase in structural lifetime.

The thrust efficiency η is also displayed as a function of the reduced frequency in fig. 12. All curves show improved characteristics with increasing k_o . For the same reasons as above, no maxima can be obtained. Nevertheless, the most flexible foil is clearly advantageous over the whole examined range, delivering an improvement ranging from 35% (high k_o) to 75% (low k_o).

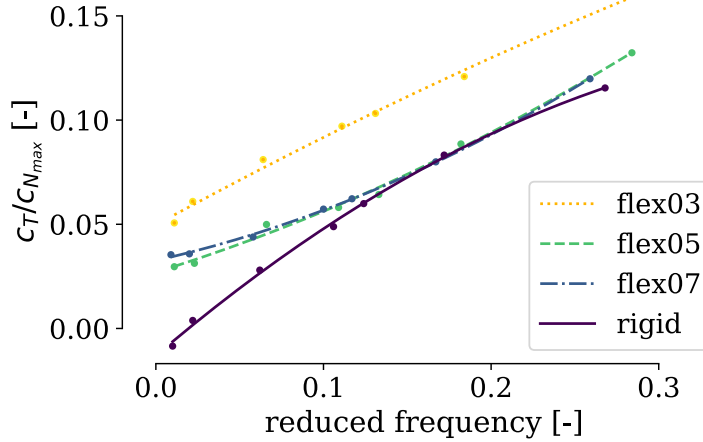


Figure 12: Thrust-to-normal-force ratio η , a measure for the benefit-to-cost ratio, as a function of reduced frequency. $\lambda=2$ for four NACA0018 hydrofoils: one rigid and three flexible foils with different blade thicknesses: [0.3, 0.5, 0.7] mm.

4.2 Results for $\lambda = 3$

The motion law for $\lambda=3$ (eq.2) results in a maximum angle $\alpha_{\max}=20^\circ$. The setup for $\lambda=3$ begins at $k_o=0.033$; the reduced frequency is then increased step-wise until it reaches $k_o=0.653$.

For all measurements carried out at $\lambda=3$, the measured drag for the first half of the period is partially negative. This unphysical behavior is a consequence of the sensor's cross-talk and hysteresis, combined with the low magnitude of the forces (see section 3 for details).

4.2.1 Transitional/dynamic state with dynamic stall at $k_o=0.069$ (fig. 13 (left)):

Rigid hydrofoil: Lift increases together with angle of attack up to the static stall angle $\alpha_{\text{stall}} = 15^\circ$, reaching a wide and smooth maximum. An abrupt peak is visible at α_{\max} on both the ascending and descending branches. From this point on, the lift reduces until the flow reattaches at the zero-crossing, where the lift is zero. Differences with the $\lambda=2$ case displayed in fig. 9, where the stall occurred far before α_{\max} , are a consequence of the different maximum angle,

but may also be affected by the higher value of k_o .

The drag features a peak at the stall point, whose magnitude in the ascending branch is 55% larger than in the descending branch.

Flexible hydrofoils: The lift curves are smoothed out compared to those of the rigid foil. The lift developed by the most flexible foil slightly overtakes that of the rigid foil. All foils develop zero lift at the zero crossing.

4.2.2 Dynamic state at $k_o=0.130$ (fig. 13 (right)):

Rigid hydrofoil: The lift reaches a larger maximum ($c_{L\max}=1.6$) at a higher angle ($\alpha=19^\circ$) than at the lower-frequency case. The dynamic stall characteristics are less significant; however, hysteresis with negative lift at zero-crossing, and smoother characteristic lift and drag peaks at the stall point can be reported, particularly in the ascending branch.

Flexible hydrofoils: The lift curves are smoothed out for all flexible foils, except for the intermediate foil ($t=0.5$ mm) which features a stall peak shortly before α_{\max} . The most flexible foil ($t=0.3$ mm) provides slightly higher lift than the rigid foil, al-

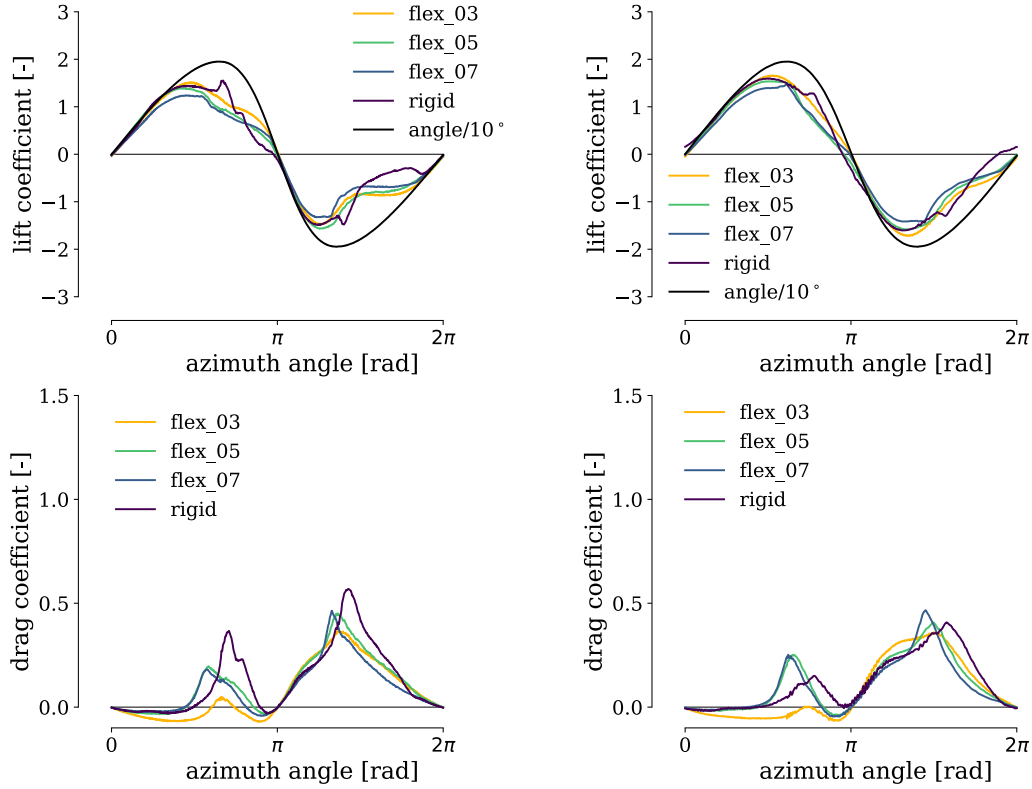


Figure 13: Results at $\lambda=3$ for four NACA0018 hydrofoils: one rigid and three flexible foils with different blade thicknesses: [0.3, 0.5, 0.7] mm. The black sinusoidal curve in the upper plots displays the angle of attack α [$^{\circ}/10^{\circ}$], with $\alpha_{\max}=20^{\circ}$. Left: Transitional state at $k_o=0.069$; Right: Dynamic state at $k_o=0.130$;

though the increase remains below the measurement uncertainty.

The drag peak for the two most rigid flexible foils is higher and occurs earlier than for the rigid foil, especially in the ascending branch. The highest drag peak is provided by the intermediary foil in the ascending branch.

4.2.3 Fully-dynamic state at $k_o = 0.241 - 0.653$ (figs. 14-15):

Starting from $k_o=0.13$, the fully-dynamic state is reached, and the maximum angle of attack $\alpha_{\max}=20^{\circ}$ is no longer sufficient to cause the hydrofoil to stall. The dominant factors are the resonant high-frequency oscillations, which require further investigations. Neglecting those oscillations, the dif-

ferences in lift and drag coefficient trajectories for $k_o=0.344$ to 0.653 remain in the range of the measurement uncertainty.

4.2.4 Performance and lifetime improvements

Figure 16 again displays the average torque coefficient for one rotation as a function of the reduced frequency. Results are similar to the case for $\lambda=2$ displayed earlier in fig. 11: the most flexible hydrofoil performs best. The maximum thrust coefficient at $k_o=0.35$ is obtained with the most flexible foil, with $c_T=0.2$. Nevertheless, the differences between all foils in both figures 16& 17 are small: the results may not be significant and have to be taken with caution. At

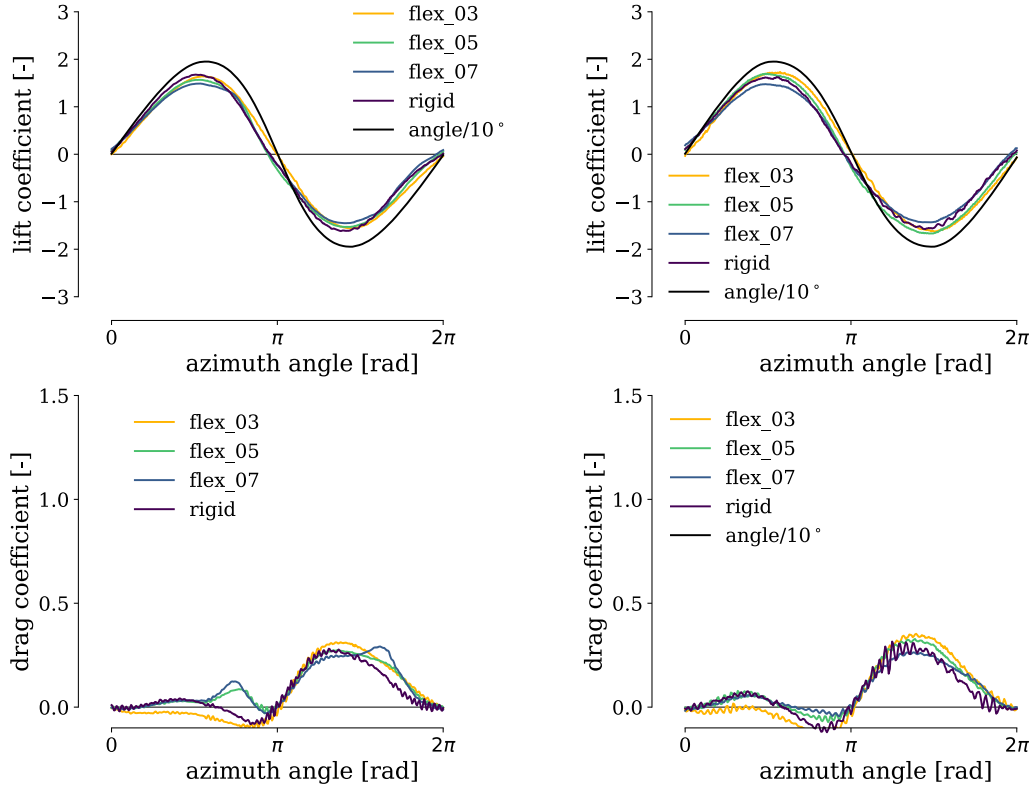


Figure 14: Results at $\lambda=3$ for four NACA0018 hydrofoils: one rigid and three flexible foils with different blade thicknesses: [0.3, 0.5, 0.7] mm. The black sinusoidal curve in the upper plots displays the angle of attack α [$^{\circ}/10^{\circ}$], with $\alpha_{\max}=20^{\circ}$. Left: Fully-dynamic state at $k_o=0.241$; Right: Fully-dynamic state at $k_o=0.344$;

$\lambda=3$ it is probable that strut and tip losses, blade-blade interaction effects and friction would exceed the thrust for high reduced frequencies, which correspond to high turbine solidity.

Figure 16 (right) displays the value of \hat{c}_N for all four foils: no influence of flexibility on the lifetime is evidenced in the case $\lambda=3$.

Finally, the thrust-to-normal-force ratio η is shown in fig. 17. The rigid foil displays a steep trend, with magnitude similar to that of the most flexible foil at $k_o=0.35$. For both lower and higher values of k_o , the flexible foil provides better performance.

5 Conclusions

The effect of blade flexibility on the performance of VAWT has been investigated experimentally in this study, particularly in regimes featuring dynamic stall. The main results may be summarized as follows:

- At $\lambda=2$ a significant improvement in the delivered thrust is observed when using the most flexible foil. This is in accordance with McPhee and Beyene [25] who studied a three-bladed vertical-axis wind turbine numerically and reported a significant improvement of the rotor efficiency. The most flexible blade provided the highest improvement. This advantage reduces with increasing values of

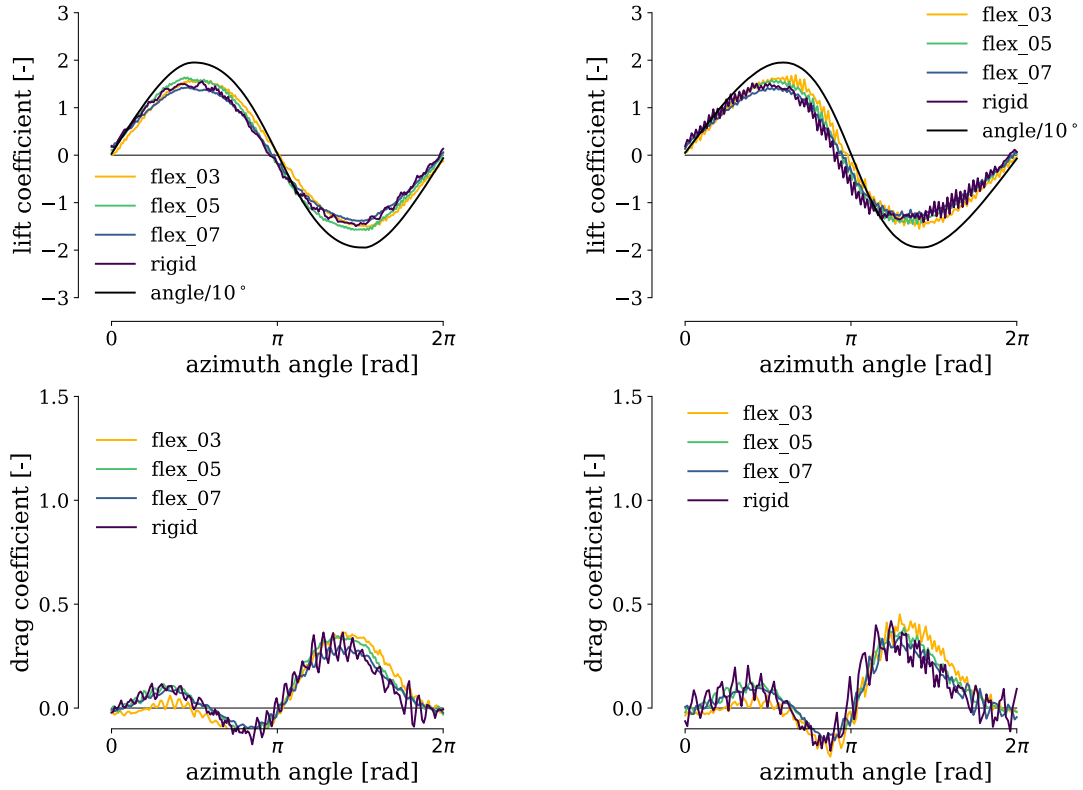


Figure 15: Results at $\lambda=3$ for four NACA0018 hydrofoils: one rigid and three flexible foils with different blade thicknesses: [0.3, 0.5, 0.7] mm. The black sinusoidal curve in the upper plots displays the angle of attack α [$^{\circ}/10^{\circ}$], with $\alpha_{\max}=20^{\circ}$. Left: Fully-dynamic state at $k_o=0.486$; Right: Fully-dynamic state at $k_o=0.653$;

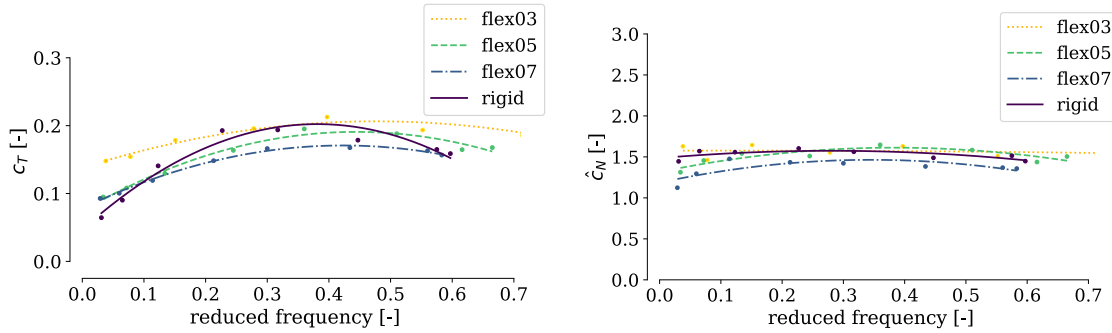


Figure 16: Left: Thrust coefficient, a measure for the qualitative performance, as a function of reduced frequency. Right: Amplitude of the normal coefficient (\hat{C}_N), an indicator for the turbine lifetime, as a function of the reduced frequency k_o . Lower values are favorable, since lifetime rises exponentially with diminishing stress; A second-order polynomial curve fit of the data was added. Results at $\lambda=3$ for four NACA0018 hydrofoils: one rigid and three flexible foils with different blade thicknesses: [0.3, 0.5, 0.7] mm.

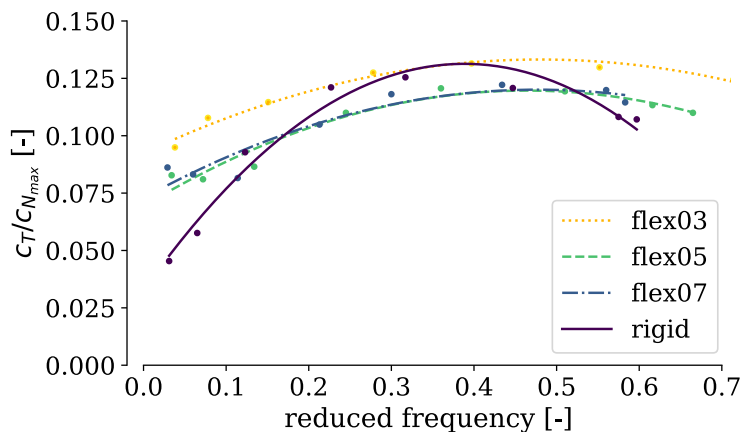


Figure 17: Thrust-to-normal-force ratio η , a measure for the benefit-to-cost ratio, as a function of reduced frequency. Results at $\lambda=3$ for four NACA0018 hydrofoils: one rigid and three flexible foils with different blade thicknesses: [0.3, 0.5, 0.7] mm.

k_o , so that the foil with intermediate flexibility becomes more advantageous for higher values of k_o . Very significant improvements in both the thrust-to-normal-force ratio and stress reduction are observed when using the most flexible foil. These improvements are explained by the lift and drag measurements, which show that much lower levels of drag and significantly smoother drag variations are obtained near the stall region, while the reduction in lift is comparatively small.

- At high tip speed ratio ($\lambda=3$), a minor advantage is seen when using highly flexible foils, particularly so at high and low reduced frequencies. Nevertheless, the low magnitude of the hydrodynamic forces results in relatively high experimental uncertainty for $\lambda=3$, so that these observations must be taken with caution. The benefits of the bending mechanism for the flexible foil are also less significant as the maximum angle of incidence diminishes with raising λ .

These results support following conclu-

sions:

1. The surrogate model used in this and in previous studies permits the detailed study of parameters such as blade flexibility over a very wide range of design points, reproducing the flow regimes corresponding to multiple tip speed ratios and turbine solidities through the choice of the reduced frequency and the oscillation trajectory. It allows relating improvements in performance indicators (c_T , η , \hat{c}_N) to the fluid dynamic properties found in the reference frame of the blade (c_L and c_D curves).

In the present case, the benefit of using a flexible structure for a given operating point may be assessed simply by reporting c_T values from figs. 11(left and right) into the design parameter map in fig. 5. However, the comparison between multiple design or operating points (k_o and λ) requires a transformation of the results in the turbine reference frame, which would include different rotational speeds as a function of λ and R , and of torque as a function of c_T and R , which depend on the design point. Then, sec-

ondary effects (upstream wake in the downstream part of the rotor, blade-blade interaction) would play a significant role.

2. Blade flexibility delivers promising improvements to the operational characteristics of VAWT. At commonly employed tip speed ratios, where dynamic stall and strong hysteresis become dominant flow phenomena, blades with high flexibility deliver significantly higher torque. This is due to their favorable behavior near the stall region, where they feature lower drag at comparable levels of lift.
3. The flexibility in VAWT blades translates into large increases in thrust efficiency (thrust-to-normal-force ratio), reducing the inner structural loads associated with normal forces. They also feature significantly reduced stress amplitude (average amplitude concerning cyclic variations of normal force), which translates into reduced fatigue-related lifetime limitations if the profile design is adapted to provide enough contributing cross-section area to distribute the force over the structure.

Further work should include a broader range of operation, with a quantitative translation of blade performance parameters into the turbine reference frame. This would allow the exploration of a wider range of turbine designs, and the identification of optimal blade stiffness (present data suggests that this is a function of reduced frequency). Furthermore, using particle image velocimetry measurements as well as surface-tracking methods would deepen our understanding of the fluid and structural dynamics of the deforming blades.

Acknowledgements

The corresponding author is grateful for the funding of his thesis by the Rosa-

Luxemburg-Stiftung Berlin, the Wachstums-kern Flusstrom Plus project, financed by the German Federal Ministry of Education and Research, and the funding of German-French-University Saarbrücken.

The authors thank the Unité Mixte de Service Grenoble-Alpes Recherche Infrastructure et Calcul Intensif et de Données (UMS-GRICAD) for their services. The support of Michael Haarman (CATLAB, Berlin), Michel Riondet and Jean-Marc Barnoud (LEGI, Grenoble) is gratefully acknowledged.

References

- [1] Erwin Amet, Thierry Maître, Christian Pellone, and Jean-Luc Archard. 2D numerical simulations of blade-vortex interaction in a Darrieus turbine. *American Society of Mechanical Engineers*, 131:15, 2009. doi:10.1115/1.4000258.
- [2] Abul Basar M Baki, David Z Zhu, Andrew Harwood, Adam Lewis, and Katie Healey. Rock-weir fishway I: flow regimes and hydraulic characteristics. *Journal of Ecohydraulics*, 2(2):122–141, 2017. doi:0.1080/24705357.2017.1369182.
- [3] Abul Basar M Baki, David Z Zhu, Andrew Harwood, Adam Lewis, and Katie Healey. Rock-weir fishway II: design evaluation and considerations. *Journal of Ecohydraulics*, 2(2):142–152, 2017. doi:10.1080/24705357.2017.1369183.
- [4] Ian D. Brownstein, Matthias Kinzel, and John O. Dabiri. Performance enhancement of downstream vertical-axis wind turbines. *Journal of Renewable and Sustainable Energy*, 8:053306, 2016. doi:10.1063/1.4964311.
- [5] Enrique Castillo and Alfonso Fernandez-Canteli. *A Unified Sta-*

- tistical Methodology for Modeling Fatigue Damage*. Springer, 2009.
- [6] Olivier Cleynen, Stefan Hoerner, and Dominique Thévenin. Characterization of hydraulic power in free-stream installations. *International Journal of Rotating Machinery*, 2017(Article ID 9806278):10, 2017. doi:10.1155/2017/9806278.
- [7] John O. Dabiri. Potential order-of-magnitude enhancement of wind farm power density via counter-rotating vertical-axis wind turbine arrays. *Journal of Renewable and Sustainable Energy*, 3(4):043104, 2011. doi:10.1063/1.3608170.
- [8] László Daróczy, Gábor Janiga, Klaus Petrasch, Michael Webner, and Dominique Thévenin. Comparative analysis of turbulence models for the aerodynamic simulation of H-Darrieus rotors. *Energy*, 90:680–690, 2015. doi:10.1016/j.energy.2015.07.102.
- [9] László Daróczy, Gábor Janiga, and Dominique Thévenin. Correlation of the power coefficients of H-darrieus wind turbines obtained using different turbulence models in CFD computations. In *the 16th International Conference on Fluid Flow Technologies*, 2015.
- [10] László Daróczy, Gábor Janiga, and Dominique Thévenin. Computational fluid dynamics based shape optimization of airfoil geometry for an H-rotor using a genetic algorithm. *Engineering Optimization*, 50(9):1483–1499, 2018. doi:10.1080/0305215X.2017.1409350.
- [11] P. Deglaire, S. Engblom, O. Ågren, and H. Bernhoff. Analytical solutions for a single blade in vertical axis turbine motion in two-dimensions. *European Journal of Mechanics - B/Fluids*, 28(4):506 – 520, 2009. doi:https://doi.org/10.1016/j.euromechflu.2008.11.004.
- [12] C J Simão Ferreira, H Bijl, G van Bussel, and G van Kuik. Simulating Dynamic Stall in a 2D VAWT: Modeling strategy, verification and validation with Particle Image Velocimetry data. *Journal of Physics: Conference Series*, 75(1):012023, 2007. doi:10.1088/1742-6596/75/1/012023.
- [13] C.S. Ferreira, R. Kemp, A. Zanon, M. Barone, and P. Giannattasio. Airfoil optimization for stall regulated vertical axis wind turbines. In *33rd Wind Energy Symposium*, 2015. doi:10.2514/6.2015-0722.
- [14] Simão Carlos Ferreira, Gijs van Kuik, Gerard van Bussel, and Fulvio Scarano. Visualization by PIV of dynamic stall on a vertical axis wind turbine. *Experiments in Fluids*, 46(1):97–108, Jan 2009. doi:10.1007/s00348-008-0543-z.
- [15] Frank E. Fish. Power output and propulsive efficiency of swimming bottlenose dolphins (*tursiops truncatus*). *Journal of Experimental Biology*, 183:179–193, August 1993.
- [16] Nobuyuki Fujisawa and Satoshi Shibuya. Observations of dynamic stall on Darrieus wind turbine blades. *Journal of Wind Engineering and Industrial Aerodynamics*, 89:201–214, 2001. doi:10.1016/s0167-6105(00)00062-3.
- [17] J. M. R. Gorle, L. Chatellier, F. Pons, and M. Ba. Flow and performance analysis of H-Darrieus hydroturbine in a confined flow: A computational and experimental study. *Journal of Fluids and Structures*, 66:382–402, October 2016. doi:10.1016/j.jfluidstructs.2016.08.003.
- [18] J.M.R. Gorle, S. Bardwell, L. Chatellier, F. Pons, M. Ba, and G. Pineau. PIV investigation of the flow across a Darrieus water turbine. In *17th International Symposium on Applications of*

- Laser Techniques to Fluid Mechanics - Lisbon*, 2014.
- [19] I. Hashem and M.H. Mohamed. Aerodynamic performance enhancements of h-rotor darrieus wind turbine. *Energy*, 142:531 – 545, 2018. doi:<https://doi.org/10.1016/j.energy.2017.10.036>.
- [20] Martin Hepperle. JavaFoil – Analysis of Airfoils, 2018. URL: <https://www.mh-aerotoools.de/airfoils/javafafoil.htm>.
- [21] A. Laneville and P. Vittecoq. Dynamic stall: The case of the vertical axis wind turbine. *Journal of Solar Energy Engineering, Transactions of ASME*, 108:140–145, May 1986. doi:10.1115/1.3268081.
- [22] L. Lazauskas and B.K. Kirke. Modelling passive variable pitch cross flow hydrokinetic turbines to maximize performance and smooth operation. *Renewable Energy*, 45:41–50, 2012. doi:10.1016/j.renene.2012.02.005.
- [23] K. H. Ly and V.A.L Chasteau. Experiments on an oscillating aerofoil and applications to wind-energy converters. *Journal of Energy*, 5(2):116–121, 1981. doi:10.2514/3.62511.
- [24] David W. MacPhee and A. Beyene. Experimental and Fluid Structure Interaction analysis of a morphing wind turbine rotor. *Energy*, 90:1055–1065, 2015. doi:10.1016/j.energy.2015.08.016.
- [25] David W. MacPhee and A. Beyene. Fluid-structure Interaction analysis of a morphing vertical axis wind turbine. *Journal of Fluid and Structures*, 60:143–159, 2016. doi:10.1016/j.jfluidstructs.2015.10.010.
- [26] T. Maître and E. Amet. Modelling of the flow in a Darrieus water turbine: Wall grid refinement analysis and comparison with experiments. *Renewable Energy*, 51:497–512, 2013. doi:10.1016/j.renene.2012.09.030.
- [27] W.J. McCroskey. The phenomenon of dynamic stall. Technical report, NASA TM-81264, 1981.
- [28] W.J. McCroskey. *Special Opportunities in Helicopter Aerodynamics*. Springer-Verlag New York, 1986. doi:10.1007/978-1-4612-4972-6_20.
- [29] W.J. McCroskey, L.W. Carr, and K.W. McAllister. Dynamic stall experiments on oscillating airfoils. *American Institute of Aeronautics and Astronautics Journal*, (1):57–63, 1976. doi:<https://doi.org/10.2514/3.61332>.
- [30] Stephanie Müller, Olivier Cleynen, Stefan Hoerner, Nils Lichtenberg, and Dominique Thévenin. Numerical analysis of the compromise between power output and fish-friendliness in a vortex power plant. *Journal of Ecohydrodynamics*, inpress, 2018. doi:10.1080/24705357.2018.1521709.
- [31] Ion Paraschivoiu. *Wind Turbine Design: With Emphasis on Darrieus Concept*. Presses Internationales Polytechnique, 2 edition, 2002.
- [32] Rohit Patil, László Daróczy, Gábor Janiga, and Dominique Thévenin. Large eddy simulation of an H-darrieus rotor. *Energy*, 160:388–398, 2018. doi:10.1016/j.energy.2018.06.203.
- [33] N.C.K. Pawsey. *Development and evaluation of passive variable-pitch vertical axis wind turbines*. PhD thesis, School of Mechanical and Manufacturing Engineering, The University of New South Wales, 2002.
- [34] Peter F. Pelz. Upper limit for hydropower in an open-channel flow. *Journal of Hydraulic Engineering*, 137(11):1536–1542, 2011.

- [35] D.M. Rosenberg, R.A. Bodaly, and P.J. Usher. Environmental and social impacts of large scale hydro-electric development: who is listening? *Global Environmental Change*, 5:127–148, 1995. doi:10.1016/0959-3780(95)00018-j.
- [36] T. D. Ivanov, A. M. Simonović, J. S. Svorcan, O. M. Peković. VAWT optimization using genetic algorithm and CST airfoil parameterization. In *FME Transactions (2017) 45, 26-31*, 2017. doi:10.5937/fmet1701026I.
- [37] F Thönnißen, M Marnett, B Roidl, and W Schröder. A numerical analysis to evaluate betz’s law for vertical axis wind turbines. *Journal of Physics: Conference Series*, 753(2):022056, 2016. doi:10.1088/1742-6596/753/2/022056.
- [38] Bryan Tilt, Yvonne Braun, and Daming He. Social impacts of large dam projects: A comparison of international case studies and implications for best practice. *Journal of Environmental Management*, 90:249–257, 2009. doi:10.1016/j.jenvman.2008.07.030.
- [39] Z. Tukovic, P. Cardiff, A. Karac, H. Jasak, and A. Ivankovic. OpenFOAM library for fluid structure interaction. In *9th OpenFOAM Workshop*, 2014.
- [40] G.S. West and C.J. Apelt. The effects of tunnel blockage and aspect ratio on the mean flow past a circular cylinder with reynolds numbers between 10^4 and 10^5 . *Journal of Fluid Mechanics*, pages 361–377, 1982. doi:10.1017/s0022112082000202.
- [41] Robert W Whittlesey, Sebastian Liska, and John O Dabiri. Fish schooling as a basis for vertical axis wind turbine farm design. *Bioinspiration & Biomimetics*, 5(3):035005, 2010. doi:10.1088/1748-3182/5/3/035005.
- [42] Dag Herman Zeiner-Gundersen. A novel flexible foil vertical axis turbine for river, ocean and tidal applications. *Applied Energy*, 151:60–66, 2015. doi:10.1016/j.apenergy.2015.04.005.
- [43] L. Zhang, Y. Liang, E. Li, S. Zhang, and J. Guo. Vertical axis wind turbine with individual active blade pitch control. In *2012 Asia-Pacific Power and Energy Engineering Conference, APPEEC.2012.6307108*, pages 1–4, March 2012. doi:10.1109/APPEEC.2012.6307108.
- [44] L. Zhang, Y. Liang, X. Liu, and J. Guo. Effect of blade pitch angle on aerodynamic performance of straight-bladed vertical axis wind turbine. *Journal of Central South University*, 21:1417–1427, 2014.